Article

Drone-Borne Hyperspectral Monitoring of Acid Mine Drainage: An Example from the Sokolov Lignite District

Robert Jackisch * [ID], **Sandra Lorenz** [ID], **Robert Zimmermann** [ID], **Robert Möckel and Richard Gloaguen** [ID]

Helmholtz-Zentrum Dresden-Rossendorf, Helmholtz Institute Freiberg for Resource Technology, Division "Exploration Technology", Chemnitzer Str. 40, 09599 Freiberg, Germany; s.lorenz@hzdr.de (S.L.); r.zimmermann@hzdr.de (R.Z.); r.moeckel@hzdr.de (R.M.); r.gloaguen@hzdr.de (R.G.)
* Correspondence: r.jackisch@hzdr.de; Tel.: +49-351-260-4493

Abstract: This contribution explores the potential of unmanned aerial systems (UAS) to monitor areas affected by acid mine drainage (AMD). AMD is an environmental phenomenon that usually develops in the vicinity of mining operations or in post-mining landscapes. The investigated area covers a re-cultivated tailing in the Sokolov lignite district of the Czech Republic. A high abundance of AMD minerals occurs in a confined space of the selected test site and illustrates potential environmental issues. The mine waste material contains pyrite and its consecutive weathering products, mainly iron hydroxides and oxides. These affect the natural pH values of the Earth's surface. Prior research done in this area relies on satellite and airborne data, and our approach focuses on lightweight drone systems that enables rapid deployment for field campaigns and consequently-repeated surveys. High spatial image resolutions and precise target determination are additional advantages. Four field and flight campaigns were conducted from April to September 2016. For validation, the waste heap was probed in situ for pH, X-ray fluorescence (XRF), and reflectance spectrometry. Ground truth was achieved by collecting samples that were characterized for pH, X-ray diffraction, and XRF in laboratory conditions. Hyperspectral data were processed and corrected for atmospheric, topographic, and illumination effects using accurate digital elevation models (DEMs). High-resolution point clouds and DEMs were built from drone-borne RGB data using structure-from-motion multi-view-stereo photogrammetry. The supervised classification of hyperspectral image (HSI) data suggests the presence of jarosite and goethite minerals associated with the acidic environmental conditions (pH range 2.3–2.8 in situ). We identified specific iron absorption bands in the UAS-HSI data. These features were confirmed by ground-truth spectroscopy. The distribution of in situ pH data validates the UAS-based mineral classification results. Evaluation of the applied methods demonstrates that drone surveying is a fast, non-invasive, inexpensive technique for multi-temporal environmental monitoring of post-mining landscapes.

Keywords: hyperspectral; remote sensing; unmanned aerial system; acid mine drainage; iron minerals; image classification; Sokolov; post-mining

1. Introduction

Acid mine drainage (AMD) is a common side-effect of the process of coal and ore mining, especially in open-pit mining. The exposition of sulfide-bearing minerals, such as pyrite or marcasite, to atmospheric oxygen and water results in their oxidation and the release of ions, such as H^+, Fe^{2+}, and SO_4^{2-}. The solution of these oxidation products in water leads to the formation of acids, which can lower the pH value of the affected environment to extreme levels. Additionally, iron-bearing secondary minerals precipitate, moderated by factors such as pH, redox potential, degree of oxidation,

temperature, and mineral content in solution [1]. The resulting secondary minerals that can be found in sulfidic mine wastes are diverse, comprising various compounds and complexes. Acid mine waters are a health risk for miners and can clog, damage, and ultimately destroy field equipment (e.g., pumps, pipework, valves, and generators). The cleaning and remediation of such waters is bound to high investments. The processing and cleaning of aqueous solutions and the disposal of tailings is regarded as a critical issue in today's mining business [2]. Vegetation, atmosphere, microorganisms, and clay content influence the pH value of soil. The natural buffer systems cannot keep the usually-balanced pH value in AMD-influenced soils and waters at natural levels. The release and mobility of plant nutrients is influenced by soil pH. Extreme pH values and high mineralization in waters can lead to a critical surplus or deficit of those nutrients. A pH ranging from 2–4 in such an environment is able to release metals and metalloids (e.g., Fe, Al, Cu, Pb, Cd, Co, As), as well as sulfates from the soil, increasing the toxic potential for agriculture, aquifers, and the biosphere [3].

We see a demand to mitigate AMD risk by applying a fast and reasonable mapping approach, based on HSI UAS-based techniques. The development and application of AMD monitoring approaches in active and abandoned mining sites has been subject of numerous studies. Especially, AMD detection and mapping using multi- and hyperspectral image data has gained popularity, since the most common secondary AMD minerals have distinctive absorption features within the visible, and up to the shortwave infrared region, of the electromagnetic spectrum, due to crystal field effects and vibrational processes [1]. Former studies focused predominantly on satellite imagery [4], airborne surveys [5–7], and classical on-ground investigations with handheld spectrometers [8–10]. However, these mapping approaches can lack either spatial resolution or are inflexible, and time and cost-intensive. Monitoring and protection of water reservoirs and ecosystems with a rapidly-deployable approach would be advantageous [10].

We apply an approach of hyperspectral UAS (unmanned aerial system)-based imaging to close this observational gap in geological remote sensing (Figure 1). Up to now, UAS-based mapping has been mainly used for agricultural applications [11–13], while soil monitoring and mineral mapping is still underrepresented [14]. Still, a large range of studies using hyperspectral UAS imaging systems showed its capability as a strong monitoring tool for various applications [15–17]. A very recent study [18] illustrates the complexity of hyperspectral imaging, where a push-broom sensor is used on an UAS. In that regard, a technical note of hyperspectral imaging [19] shows that only 4 out of 24 available hyperspectral sensors are snapshot-based, while the majority are line scanners.

The mapping scope of this study focused on four common AMD minerals (Table 1), which serve as proxies for low pH, acid mine waters, and mine waste byproducts. We selected the study area of Litov, Sokolov, Czech Republic due to its interesting geological and geochemical properties. The lignite waste dump is not only characterized by high AMD influence and a varying morphology, but was broadly investigated in previous studies [20–24]. By the aid of SfM-MVS (structure-from-motion multi-view-stereo) photogrammetry, ground trothing, and laboratory validation, we achieve multi-temporal, sub-decimeter resolution maps showing AMD proxies. The required geometric, radiometric and topographic corrections of drone-borne hyperspectral imagery were conducted after Jakob et al. [14]. We demonstrate that UAS-based hyperspectral mapping is a utilizable tool for environmental monitoring by high-resolution, multi-temporal mapping of iron-minerals.

Table 1. Main AMD proxies proposed of this study. Their specific absorption features are taken from several sources [8,10,25–28] and given in nm.

Mineral	Formula	Spectral Feature Position [nm]
Jarosite	$KFe_3(SO_4)(OH)_6$	436 [a], 716 [P], 920 [a], 1465 [a] 2264 [a]
Schwertmannite	$Fe_8O_8(SO_4)(OH)_6$	545 [e], 738 [P], 912 [a] 1449 [a], 1945 [a]
Goethite	$\alpha FeOOH$	484 [e], 668 [e], 760 [P], 932 [a], 1454 [a], 1944 [a]
Hematite	Fe_2O_3	586 [e], 744 [P], 868 [a]

[a] Indicated absorption maximum; [P] Indicated absorption peak; [e] Indicated absorption edge.
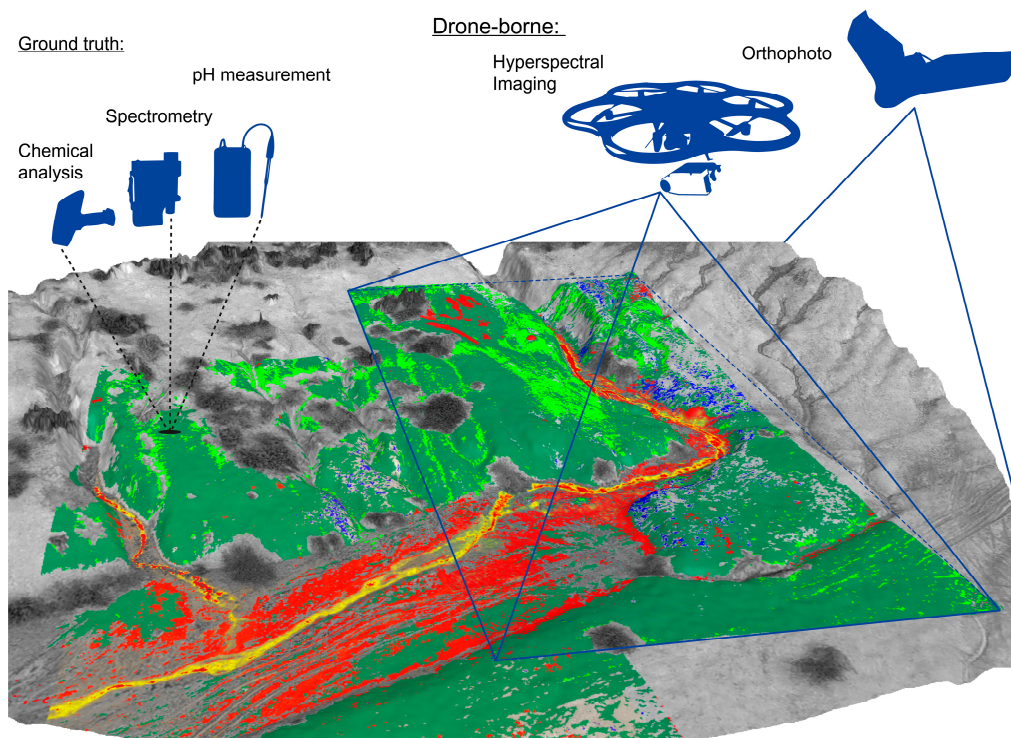
Figure 1. Workflow during the field work for the Litov campaigns. The two main working procedures, the UAS-based data acquisition (right corner) and the ground validation (left corner), are shown. Superimposed on a 3D model of the landscape are two classified HSI scenes.

Further AMD-related research using multispectral remote sensing was conducted in regions where large mining operations influence the landscape, e.g., spectroscopic investigation of iron content in surface water from mine tailings [29].

The application of earth observation techniques and remote sensing technologies plays an important role in collaborations between research facilities and the mining industry [30]. A study with the purpose to map steelworks and iron byproducts identified jarosite and other iron minerals [31], achieving promising results with a hyperspectral mapping approach and endmembers deviated from image scenes in combination with geochemical validation.

2. Study Area

The chosen test area to conduct this study is the Litov tailing lake and its adjacent waste heap, situated in the Sokolov district of the Czech Republic (Figure 2). The site is situated between the village Chlum Svaté Maří in the south and the borough of Litov in the north. The Sokolov basin is part of the Eger-Rift, an inactive rift and part of the European Cenozoic rift system, originated from the remote influence of Alpine orogenic activity and uplift [32]. The basin is up to 400 m deep and dates back to the Oligocene–Miocene, with the Cypris Formation as the youngest tertiary sediment formation [33]. The exploited coal seams Josef, Anežka, and Antonin contain sulfur between 5–8 wt %. Mining in the area began in the 17th century [34], and lignite mining started roughly a century later. Growing fuel demand led to extended open-pit mining. Although, only a few mines are still active today, mining activities changed the appearance of the regional landscape. The Litov dumpsite is exemplary for the anthropogenic footprint of resource extraction activities and deposition of overburden material caused by open-pit mining. The waste heap covers a surface area of 7.2 km^2 and contains a volume of 0.22 km^3 of overburden and waste material from the nearby former mine of Habartov. The piled material reaches an average height of 570 m above sea level.
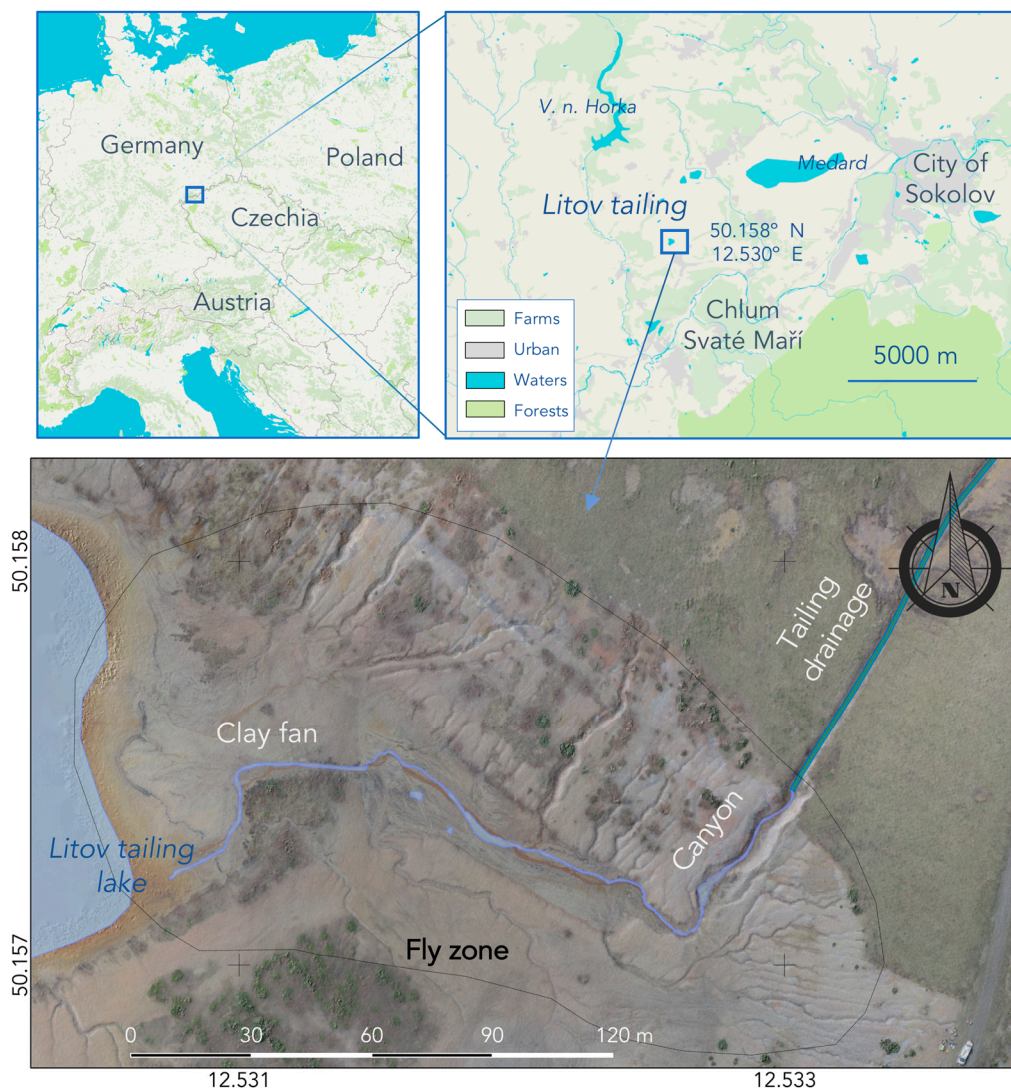
Figure 2. Location of test site in the district of Sokolov. The orthophoto was captured with the eBee UAV. Within the re-cultivated area is the actual tailing, east of the lake. Black arrows indicate dominant drainage directions. Collected orthophotos cover up to 0.635 km^2, or 8.9%, of the waste heap. The region is part of the educational Czech-Bavarian Geopark.

A study concerning the Sokolov vegetation found pH values ranging from 2.3–2.9 in the same area [35] and defines Litov as the site with the lowest occurring average pH values of the Sokolov mine sites [21]. The authors emphasize the acidity of the Litov dumpsite and mapped the occurrences of the minerals we expected to investigate during the investigation. The proposed minerals in Table 1 serve as proxies for UAS spectroscopy and are used for the validation in subsequent field spectroscopy, as well as XRD analysis. Their specific absorption characteristics during reflectance spectroscopy give them distinguishable spectral patterns [10,26,36].

3. Data and Methods

3.1. Hyperspectral Camera and UAS Setup

The HSI are obtained with the Rikola hyperspectral camera, a full-frame lightweight device from Senop Oy, Kangasala, Finland providing the camera [37]. The specific properties of the Rikola camera are given in Table 2.

Table 2. Technical setting of the Rikola camera, as used in the field and laboratory.

Parameter	Value
FOV	36.5°
Spectral range	504–900 nm
Spectral resolution	~10 nm, FWHM
Spectral bands	50 [D], 80 [L]
Integration time per band	10–50 ms, depends on light conditions
Pixel resolution	1010×624 [D], 1010×1010 [L]
Weight	720 g

[D] Drone-borne; [L] Laboratory (increased feasibility).

The HSIs require a series of pre-processing steps, which are discussed in a precursor study to this work [14], depicted in Figure 4. The workflow and measurements to obtain co-registered, georeferenced, and topographically-corrected HSI is described in detail in the publication. We use the in-house developed toolbox, which allows the processing, as well as the correction of these kind of drone-borne data to create corrected, comparable HSI scenes. Automatic georeferencing of single HSI scenes to the reference system WGS 84 UTM 33 N is carried out via image matching. The atmospheric correction and the conversion from radiance to reflectance of the HSI spectra is achieved with a basic empirical line approach [14]. We use spectrally-defined ground targets, such as PVC panels in white, grey, and black on the ground for calibration. The calibrated reflectance spectra were examined and smoothed with a Savitzky-Golay filter [38] and variable moving window sizes.

We sampled 160 ground points during the four campaigns. Ground spectroscopy is carried out with the Spectral Evolution PSR 3500 portable spectrometer, which features a spectral range of 350–2500 nm. It was calibrated with a Spectralon (SRS-99) white target [39]. Soil samples (500–1000 g) were taken for all sample points, respectively. Their locations were surveyed with a Trimble R4/2 GNSS unit and later post-processed with a local base station (Trimble R5) and the SOPAC network to achieve 3–5 cm ground position accuracy.

3.2. UAS Settings

We used two different UASs for specific tasks. The UAS properties are given in Table 3. An Aibotix Aibot X6v2 hexacopter carried the Rikola hyperspectral camera. This UAS is well-suited for hyperspectral image acquisition. An integrated gimbal steadies the camera while the data is taken over a predefined target spot. Flight automation was achieved via the creation of a GPS point profile in the UAS software. All campaigns but one are flown along similar flight lines. We conducted the second campaign in manual flight mode because of a software issue. We see the advantage of a copter in its ability to fly snapshot cameras and stop midair over a target. Especially, when facing a mine wall or slope, the camera could be rotated to face the wall for imaging. We did not extract IMU (inertial measurement unit) position data, as we assume that all HSI are in the nadir position. The Aibot can land automatically, but the pilot preferred to land the copter by remote control. This ensures a better protection of the expensive HS camera. The Aibot features installations to protect the payload, via ground and side-distance measurements via ultrasonic distance measurement. The fixed wing sensefly eBee UAS took orthophotos, and by the aid of SfM-MVS photogrammetry in Agisoft Photoscan [40], we created referenced digital elevation models. Flights for SfM-MVS were executed with 90% horizontal and 70% vertical image overlap, to compute the elevation models. The advantage of the eBee is its high flight endurance of >50 min and, therefore, the capability to cover large areas. The images and flight logs (GPS points of stops and flights) of both platforms are stored internally.

Table 3. UAS properties used for the Litov study. F = Flights; I = Images.

Parameter	Aibot X6 V2 Hexacopter	eBee Fixed Wing
Camera system	Rikola	Canon Powershot S110 RGB
Flight duration	8–15 min	15–25 min
Weight	5 kg	700 g
Altitude	50 m	120 m
Area covered per flight	6000–10,000 m^2	0.6 km^2
Shutter time	10–25 ms	10–50 ms, depending on light
Resolution on ground	3–5 cm	5–15 cm
Sensor resolution	1010 × 624 Pix	12 MPix
April: F/I	3/20 **	1/227
May: F/I	2/34	1 */104
July: F/I	1/23	1/125
September: F/I	2/41	1/204

* Acquired with a GoPro Hero 4 RGB 12 MPix camera on a DJI Phantom 2 UAS; ** Before Rikola firmware update only 19 spectral bands in autonoumous mode.

3.3. Laboratory Spectroscopy

We conducted further investigations of the target spectra with the Rikola instrument under laboratory conditions. For this procedure, we scanned prepared target sample trays, assembled in groups of three to four with the Rikola instrument. The calibration panels had to be present inside the image frame, for later conversion to reflectance. To refine the process, we chose a wide range of wavelength settings and integration time steps. The image processing consisted of the same procedures as with the drone-borne images. Due to the short sample–sensor distance, we selected a larger smoothing window, from stepsize 6–8, with a third-order polynomial.

3.4. pH Measurements

We acquired the pH values according to DIN ISO 10390:2005 [41] with a Knick Calimatic pH meter 766. Measurement with a KCl or NaCl solution in soil suspensions deliver lower pH values (pH reduced 0.5–1 units) then compared to the standard measurement with distilled water. However, the fact that a part of the samples contained enough suspension to measure them undiluted, we decided to go with distilled water suspensions, which mirrors the in situ properties.

3.5. Band Ratios and Classifications

A basic indicator for absorption features is the band ratio. The division of one band by another gives an indication for absorption or reflection. We selected band ratios from the Rikola instrument for the Fe-indicating reflectance peak around 710–760 nm and the NIR region of 870–890 nm, that is the band cap of the Rikola instrument. A band-ratio >1.0 indicates an iron absorption feature, which could be correlated with XRF data for Fe. A more sophisticated band ratio, the NDVI [42] is applied on the HSIs to mask out vegetation.

The spectral angle mapper (SAM) is a supervised image classifier, measuring the similarity between a reference and a target spectrum. The spectral angle between two spectra is calculated from the two spectra in an n-dimensional (n = number of bands) coordinate system [43]. With only the curve shape as important factor, the SAM algorithm made a robust tool for different illuminations which occurred in our study. The smaller the angle in radians (rad) between two spectra, the higher the similarity. Reference values are scarce, therefore, we relied on very small SAM values between 0.05–0.08 rad for the classifications.

3.6. Mineralogical and Geochemical Sample Evaluation

We characterized field samples by portable X-ray fluorescence analysis (pXRF) and XRD. Dried, representative sample fractions were mixed with 10 mL ethanol and milled in a McCrone micronizing

mill down to approximately 4 μm grain size. A PANalytical Empyrean X-ray diffractometer with a Co anode, and a Pixcel 3D medipix3 detector is used for XRD readings. A handheld XRF Bruker S1 Titan 800 with a Rh anode was utilized for XRF measurements in the field and laboratory. Surfaces were homogenized prior to measurement. An integrations time of 60 s was chosen, allowing for reasonable detection limits.

3.7. Defining the Spectral Endmembers

According to the aforementioned steps, we built the endmember library from four remaining target spectra, defining the main character of the area. We use them for the supervised classifications. Visible in Figure 3 are the target samples for the endmember extraction. The procedure to acquire them was as follows (Figure 4):

1   Select fitting samples, visible in at least one HSI with pH value between 2 and 5;
2   Samples typify one characteristic surface feature, e.g., an iron-rich hardpan;
3   Obtain XRF or XRD values and a continuous spectrum from 350–2500 nm, 1024 bands;
4   Scan samples in the laboratory with the Rikola camera from 504–900 nm, 50–80 bands, 20 ms integration time;
5   Extract surface spectrum of characterized samples via unsupervised classifications, e.g., k-means [37];
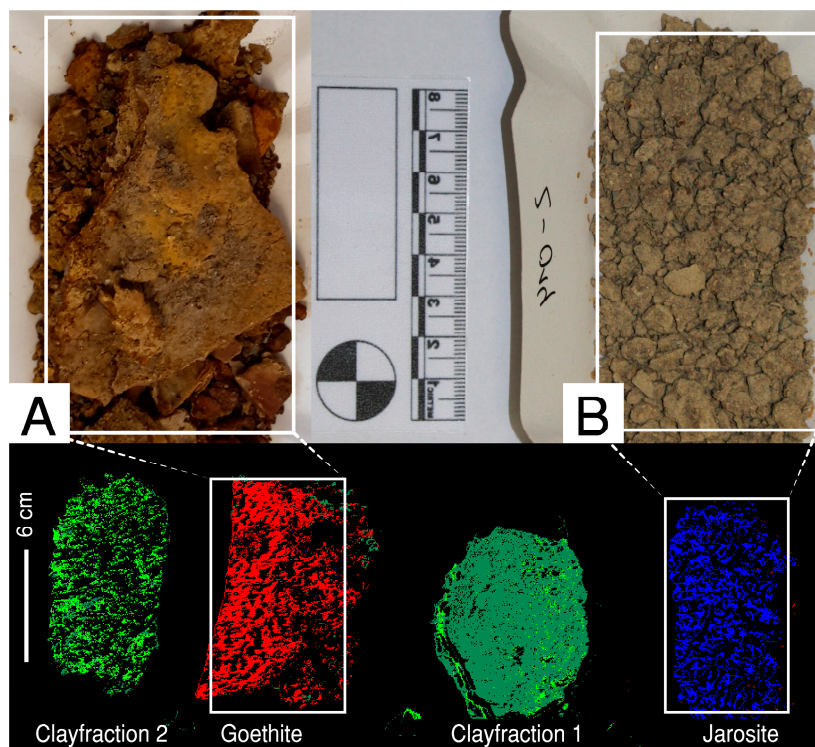6   Create the endmember spectral library with all samples, hand spectra, and library spectra for classifications.

Figure 3. (**A**,**B**) display sample trays with material from Litov, selected as training classes. For the supervised classifications, the extracted endmember are displayed below. Their averaged spectra are used for the validation. Their color codes are later assigned for the supervised classification maps. Figure 6C displays the endmember library.
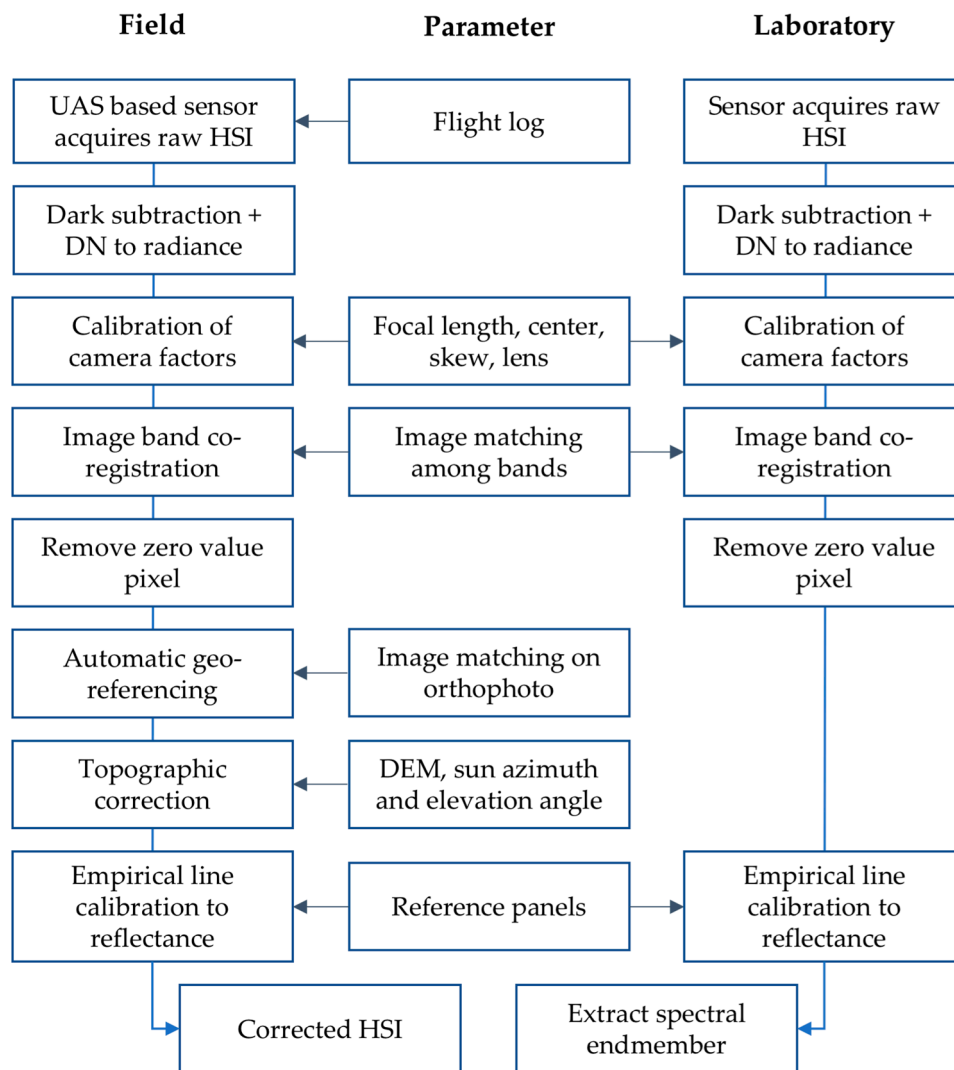
Field	Parameter	Laboratory
UAS based sensor acquires raw HSI	← Flight log	Sensor acquires raw HSI
Dark subtraction + DN to radiance		Dark subtraction + DN to radiance
Calibration of camera factors	← Focal length, center, skew, lens →	Calibration of camera factors
Image band co-registration	← Image matching among bands →	Image band co-registration
Remove zero value pixel		Remove zero value pixel
Automatic geo-referencing	← Image matching on orthophoto	
Topographic correction	← DEM, sun azimuth and elevation angle	
Empirical line calibration to reflectance	← Reference panels →	Empirical line calibration to reflectance
Corrected HSI		Extract spectral endmember

Figure 4. Flowchart showing single processing steps for HSI data.

4. Results

4.1. pH Characterization

The low pH value present in the Litov site is a key feature [44] and one major physical agent, which is shaping the mineralogy of the region. The boxplot distributions of the pH values are illustrated in Figure 5. Minimum amounts of 29 measurements were taken per campaign. We observe the overall pH-value distribution from 2.2–4.7 for all samples. The means ranged from 2.7–2.9 per month, the medians from 2.5–2.8, campaign-wise. The overall mean pH value of the monitored area was 2.8. However, the distribution in the field naturally differs, as there is a morphological gradient between two surface features.

The first of these two features is a gradual opening from a small canyon through the clay fan into the tailing lake. The clay fan had the lowest pH regions, up to the shore of the lake. The second area is the rocky surface debris surrounding the fan, with 4.7 as the highest pH value measured.
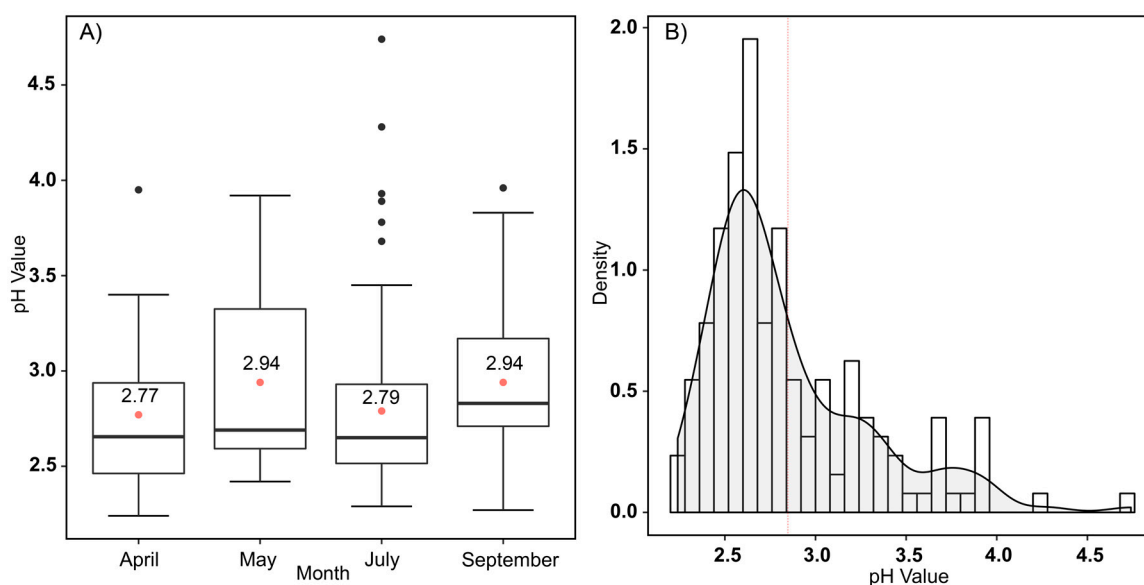
Figure 5. Displayed are the distributions of pH measurements as boxplot and histogram. The boxplots in (**A**) indicate that, for all four campaigns, 50% of the values deviate below 1 pH unit among each other. The red dot in (**A**) marks the mean per month. The histogram (**B**) spreads all measurements, in a bar view and as a density curve. The mean pH for all campaigns is 2.8.

4.2. Results of Mineralogical and Geochemical Analyses

Table 4 shows the mineral content from selected field samples. The sample ID is a combination of month and sequence of acquisition. We found a pH range from 2.4–2.7 for selected materials. The mineral composition of the region is dominated by sheet silicates, the mass fractions of their members kaolinite and muscovite in detected samples ranged from 39–65 wt %, obtained from XRD results. Around one quarter per sample was quartz, and the polymorph silicon variation cristobalite was detected, which can be a hint for the presence of opal.

Table 4. Mineral mass fractions resulting from XRD quantitative analysis of five selected samples to represent the Litov area. AMD minerals are jarosite and geothite. The estimated standard deviation is below 0.2% for each, and the pH ranges from 2.4 to 2.7 for the shown samples.

2-010	wt %	2-014	wt %	2-022	wt %	3-007	wt %	3-077	wt %
Kaolinite	55.8	Kaolinite	39.2	Kaolinite	59.8	Kaolinite	65.5	Kaolinite	48.7
Quartz	23.5	Quartz	26.6	Quartz	17.3	Quartz	17.5	Quartz	24.1
Jarosite	7.6	Jarosite	21.7	Jarosite	7.5	Jarosite	7.0	Jarosite	4.9
Goethite	2.5	Goethite	7.0	Goethite	2.8	Cristobalite	5.6	Goethite	11.1
Muscovite	5.0	Gypsum	2.1	Muscovite	7.7	Gypsum	3.1	Cristobalite	4.5
Anatase	1.9	Titanite	1.4	Crisobalite	1.5	Anatase	1.5	Muscovite	4.3
Gypsum	1.7	Muscovite	1.3	Gypsum	1.5	Rutile	0.7	Rutile	1.0
Cristobalite	1.4	Anatase	0.6	Anatase	1.4			Gypsum	0.7
								Titanite	0.5

We detected titan dioxide variations rutile, anatase, and titanite. These are typical components of sandy soil, possible indicators for heavy mineral-sands in the area, which can be found in river sediment beds. Most important, we find that goethite and jarosite dominate the AMD mineral fraction, as both are in differing amounts. Goethite dominated the classification results in the HSI maps. Former studies in the area reported similar observations, with goethite found in pH regions up to 6.5 [21]. The authors concluded that the jarosite–goethite association shows a transition stage, for a metastable mineral converting to a stable form. We could not detect schwertmannite as an AMD proxy in the area,

although we expected it in pH ranges from 3.0–4.5 [10]. Only around 25% of the collected samples were found in this pH range, but for a few spectra, schwertmannite was detected by reflectance spectroscopy. However, XRD results were unambiguous regarding schwertmannite in these cases. It was not detected once, so we ruled it out. Some samples originating from the canyon area appeared to be jarosite in spectral investigations. Hand spectroscopy of some samples indicated a good goethite resemblance, but in pH zones of 2.7. We assumed goethite/jarosite in association, but XRD analyses of one of these structures revealed goethite or jarosite with major clay components. We found hematite only in small fractions. We perceived XRF iron values for these samples from 25–39%, showing that AMD minerals occur mainly on the top layer. With very low sulfur values (5–6%) and a Fe:S ratio of 5:1, we found jarosite as the minor constituent. We saw that the bulk of these samples, particular around the stream, was goethite and the XRD results of some local features are only true for the very small top-crust. These surface crusts/needles appear to be cemented clay-quartz grains with a very thin iron coating.

We did not identify the iron-sulfide pyrite, the progenitor mineral of the AMD cycle, by XRD. We deduce that this starting material for jarosite and further minerals should be completely degraded down to other minerals. Detection via VNIR-SWIR (Visible near infrared—short wave infrared) spectroscopy is not possible for all minerals identified (Table 4). For example, quartz, feldspars, or pyrite show no characteristic absorption features in this range. Additionally, we assume that surfacing pyrite has long since degraded, and no surface material was left for detection by XRD.

We applied the handheld XRF in the field and on laboratory samples for a quick integration of basic elemental contents. The dominating elements we classified are aluminum, iron, sulfur, silicon, and titanium. Interesting for the study context are mainly iron and sulfur, as the sought-after AMD minerals are built of iron and sulfates. An indicator for jarosite is the 1.5 Fe:S ratio. One reference point is the correlation between Fe, S, and measured pH.

We observed high Si and Al content (from sheet silicates and quartz), but also increased sulfur and somewhat high iron values. The high correlation for Al and Si indicates a good fit for clay-type minerals. The highest iron content measured was 31 wt %. The results of XRD compared to XRF differ, because XRD samples were milled to be representative, and XRF scanning occurred on surface parts of the same samples. Furthermore, the XRD results are Rietveld-refined, to fit a library reflection peak profile on the measured profiles. We regard the XRD results, therefore, as calculated values.

The laboratory measurements with the handheld XRF introduced a signal attenuation. As the wet soil samples slurred the beryllium window of the XRF device, we applied a thin cling-foil between the sample and window. The X-ray passes through this polyethylene layer, so secondary radiation has to pass again through the foil. This resulted in an increased signal attenuation of secondary X-rays from the excited sample, as compared to vacuum or direct sample contact. Light elements up to the fourth periodic group are mainly affected by low-energy excitation and the X-ray response is severely reduced. We observed this effect during the scanning of the laboratory samples, especially aluminum and silicon, as light elements in compounds are affected. The detected X-ray response from excited shells has a lower energy for light compounds than for iron compounds.

We applied an XRF calibration with multiple reference standards to reduce this error. We utilized iron-specific laboratory standard samples for calibration [45,46]. A two-point calibration was conducted with these certified reference materials, where library wt % Fe was plotted against mean wt % Fe values. We deduced the calibration formula of $Fe_{corr} = 1.0128\ Fe_{raw} + 0.002718$ to correct the iron readings. We achieved a correction of 2% for the iron content of XRF, however, the results should be treated as a gradient indicator.

We conducted a visually-based comparison of the continuum removed and normal reflectance spectra based on library data [47] to sort and categorize the obtained field and laboratory spectra. We compared library and field spectra by the aid of the SAM. Exemplary for false positives is the mineral nontronite, which could not be detected by XRD, but showed a very high fit for a few

corresponding field spectra. Nontronite as sheet-silicate is rare, sometimes found in alkaline soils, and was not reported in any other study regarding the Sokolov region [34].

We chose assorted samples for specific minerals to act as proxies, according to the field spectrum, pH, mineral and iron content, surface color and location in the Litov area. Figure 5A distributes typical field and drone-borne spectra. Exemplarily marked are absorption features, typical for OH-overtones, caused by vibrational absorption with minima between 1400–1900 nm. Around 2180–2220 nm, we observe Al-OH absorption. Between 2250–2380 nm, the visible absorption is caused by Fe-OH and Mg-OH bonds [8,26]. This feature is caused by metal-OH bending, which serves as strong diagnostic property for mineralogy, especially in sheet silicates [1]. Due to the nature of the study zone, many of the probed surfaces were slightly moist, which contributes to the observed strong water absorption.

4.3. Field and UAS Spectra Combination, Resulting in the Endmember Selection

Figure 6 represents various reflectance spectra from the conducted campaigns, field and laboratory alike. Frame A displays the three principal surface materials observed in the Litov area, mostly leaves, hardpans or mineral crusts, and clays.
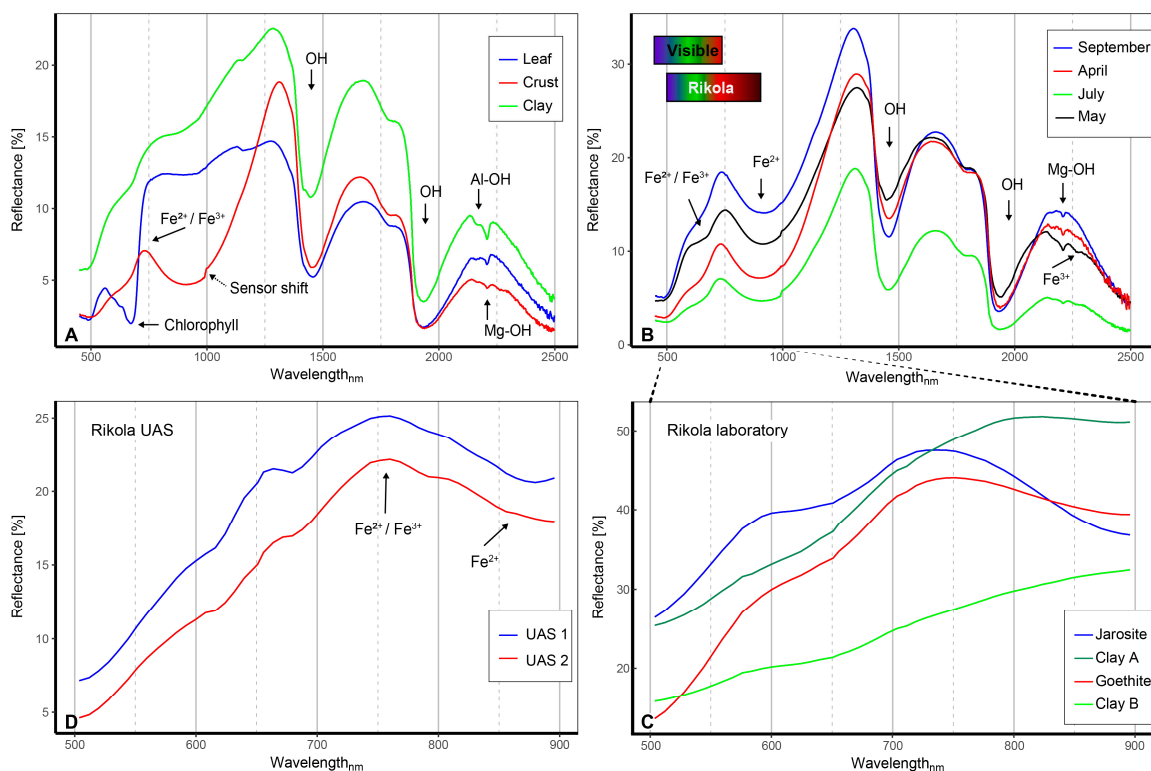

Figure 6. Examples of different spectra, selected during the Litov field campaigns. Frame (**A**,**B**) show the field spectra, obtained with the Spectral Evolution spectroradiometer. Frames (**C**,**D**) illustrate spectra acquired with the Rikola HS camera. UAS 1 and 2 refer to two different points in the same HSI.

Figure 6B exhibits well-shaped mineral specimen representing prominent iron absorption visible, e.g., from 400–950 nm. These spectra were collected during the four campaigns in high proximity to the small river. Their SAM similarity is below 0.08 rad. The shoulders left to the 900 nm trough are varying, their peak location laying between 720 and 760 nm, with 720 nm indicating jarosite, whereas 750 nm suggests hematite and 760 nm points towards goethite. This difference between 720 nm and 760 nm is further used to discriminate between jarosite and goethite in the classified Rikola UAS-borne HSIs. The representative sample features were captured under laboratory conditions. Another diagnostic small absorption feature occurs around 436 nm for jarosite and 494 nm for goethite [8,26]. We compared

the spectral field observations under repeatable settings, and scanned a wide range of field samples under laboratory conditions with the Rikola camera and the hand spectrometer. Naturally, surface conditions in the field can change within hours. We spread the solid samples evenly on cardboard trays, were store-dried, and scanned multiple times. A spectral library with the mean reflectance value per sample resulted. The iron absorption feature around 900 nm is prominently marked in most samples. The sample "May" of Figure 6B has the distinctive jarosite absorption feature at 2264 nm [48]. This feature, caused by Fe-OH vibration, is often found on pure powdered jarosite and mostly covered by broad OH-bending from topped clays. The XRD analysis of an adjacent sample (ID 2-014) contained 21% of jarosite, the highest measured value per sample. Spectral absorption features at 436 nm and 2264 nm are jarosite indicative and, therefore, substantiate it as an endmember.

We obtained the goethite endmember from a field sample surrounded by the local stream. We chose a hand-sized piece of solid crust, as it featured prominent enclosing sheets of hardened kaolinites and was covered by goethite on its surface (ID 4-023). Spectral measurements revealed a small 436 nm feature, but a steep incline at 494 nm, typically for goethite. Optical microscopy helped to discern the encrusted surface features, and showed the coalescence of the two different AMD minerals. The endmembers were compared with the obtained mean laboratory spectra from several ROIs per image. A further validation was conducted with USGS library spectra, targeting AMD minerals. USGS spectra Jarosite WS2501 and Goethite WS220 [47] serve as comparable standards.

The classification, as well as the final endmember library in a wavelength range between 504–900 nm, are shown in Figure 6C. The Rikola laboratory spectra displays the four designated endmember, applied on the UAS-borne HSIs (see upcoming section). The classification results from the lab reveals a high correlation between the observed material and library spectra.

4.4. The Rikola HSIs, Processed and Classified

HSIs resulting from the UAS Rikola are presented after processing. The HSIs can be mosaicked by the aforementioned toolbox [14]. Although first investigations were applied on stitched mosaics, single scenes delivered more accurate and coherent classification results. Single scenes were topographically corrected and georeferenced. Another advantage is their small size and, therefore, faster processing times.

Figure 7 shows the overview of the Litov area as mosaic of different scenes. The false color RGB illustrates Rikola bands 17 (630 nm), 7 (551 nm), and 1 (504 nm) to create a natural looking image. Bright illuminations in the first few scenes on the right side were caused by a small oversaturation during the image acquisition.

The May campaign was flown manually, giving the advantage of more scenes from the same spot and a higher overlap in-between the single images, but consuming more time. The images with the highest quality, in regard of light conditions and noise, were selected from this dataset for further processing. The illumination during the very first campaign was mitigated by a considerable amount of clouds, and reduced daylight. The sprouting of vegetation and the thickening of the canopy from April to September is clearly visible in the images. NDVI investigations are possible, but have not been subject of this article.

The grade of detail possible with the UAS-borne HSIs is remarkable. Figure 7 demonstrates the July mosaic his, overprinted with differently magnified HSI scenes from September. In the outcrop HSI with more detail, we can observe actual footsteps and tire carvings. Vegetation features, such as twigs and branches, are distinguishable. The pixel size of these HSIs varies between 3 and 4 cm. In the lower right corner, a 3D hypercube is shown for illustration, which indicates spectra of the canyon area. The right upper frame in image Figure 7 is a false color scene from September. The RGB color-code are bands 50 (895 nm), 30 (735 nm), and 10 (575 nm). This band combination distributes vegetation as clearly distinguishable from the unusual displayed soil color. Changing band combinations can enable the user to observe, for example, different water depths. The brightness per band can differ to a certain degree.
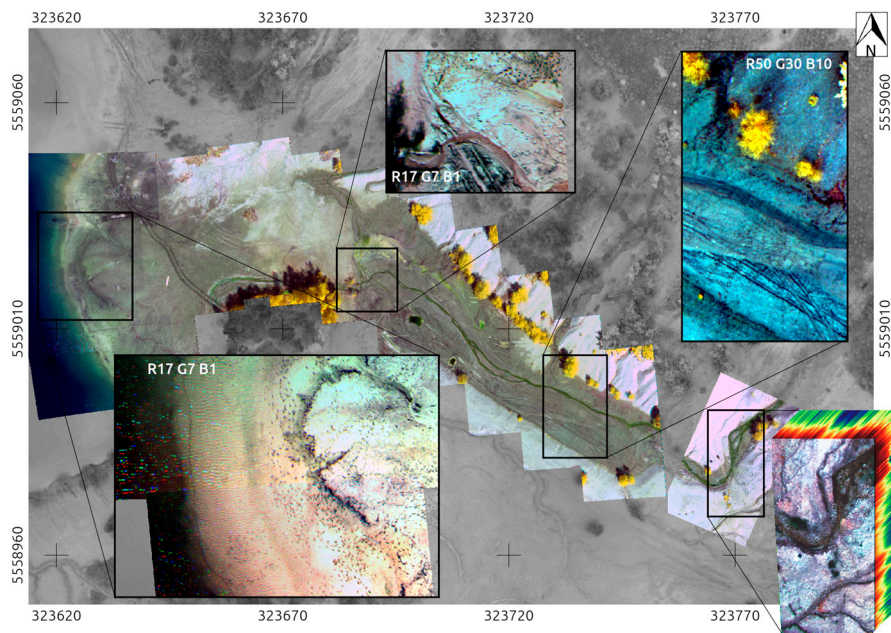
Figure 7. HSI scenes of July are superimposed with enhanced outcrops of September HSI, to showcase the level of detail. The pixel size of the HIS approximates 4 cm. Shown underneath is an orthophoto, obtained by the eBee UAS. The hypercube in the lower right corner illustrates the added spectral dimension.

4.5. Comparing the Spectral Classifications of UAS-Borne HSI

Examples of supervised classifications performed on single scenes are presented in this section. Only selected images are shown for practical reasons. We achieved compelling results by a combination of calculated band ratios and SAM classifications. Values below one are masked band ratios, as they contradict the purpose of mapping iron absorption. A decline of the reflectance values in a wavelength range from 720–880 nm (see Table 1) represented the most noticeable spectral AMD features. The band ratios in Figure 8 were calculated for 750/880 nm.
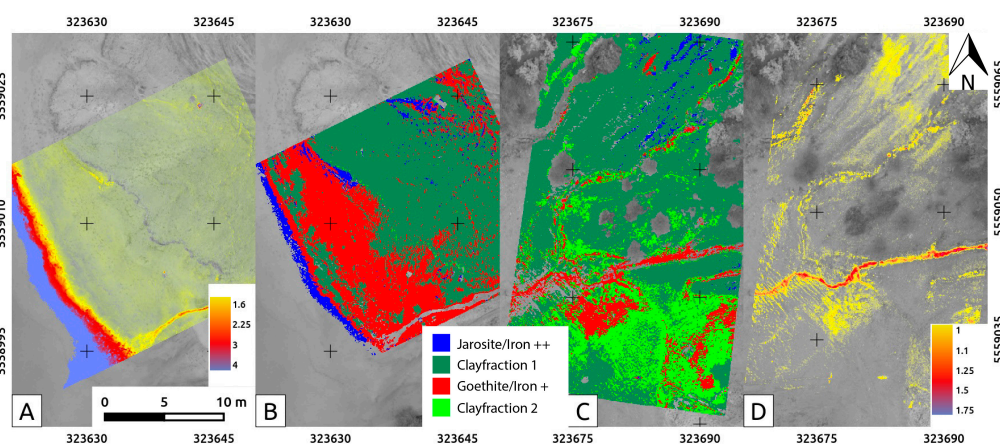

Figure 8. Results of two different classification approaches of two scenes, May 2016. Frames (**A**,**B**) display a waterfront scene, with band-ratio calculation and SAM classification, respectively. Frames (**C**,**D**) display the northern slope of the Litov area, first the SAM classification (**C**) followed by the band ratio (**D**). The endmember legend applies to (**B**,**C**). The legend in (**A**,**D**) is the dimensionless band-ratio of 720/880 nm.

The legend in frame B is valid for C, as well. The red color class is representative for the goethite endmember, blue for jarosite as the main fraction, and green with sea green are the clay–rock mixtures. Most classifications indicate that the goethite endmember, together with clay endmember 1, do occur the most in almost every scene. The goethite class constantly reached smaller SAM values during classifications, meaning a better fit.

Frame D presents a classification result with a SAM angle of 0.08 rad and all four endmembers. A remarkable feature is the stream with clear iron absorption features. A distinction between the two iron minerals goethite and jarosite is possible. The clay–rock fraction can be observed in the northern part, and smaller areas are classified as clay. The shape of the captured stream is very similar to the band ratio in frame A, but the SAM image allows a closer look at the mineral distribution in the river bed.

Figure 8 compares mapping of the west beach and slope area. The band-ratio 720/880 nm (A and D) indicate iron absorption features in the spectrum but, in this case, to a much higher degree. The legend (frame A) shows that a ratio of four is reached, a high value in regard to other band-calculations, meaning a steep decrease from 720–880 nm. The light blue area is one, particularly low reflective submerged area with presumably high iron mineral content. Additionally, the stream is recognizable in frame A. SAM, as seen in frame B, does not map the same stream feature. As the classifications indicate, the SAM algorithm could not map the stream. One reason for this might be the high water absorption due to different water tables, but also a sensor shift in the Rikola around 650 nm. This device-specific property is unfortunate in our approach, as it creates artificial absorption and reflection features, in particular in the Rikola spectrum of April in Figure 9.
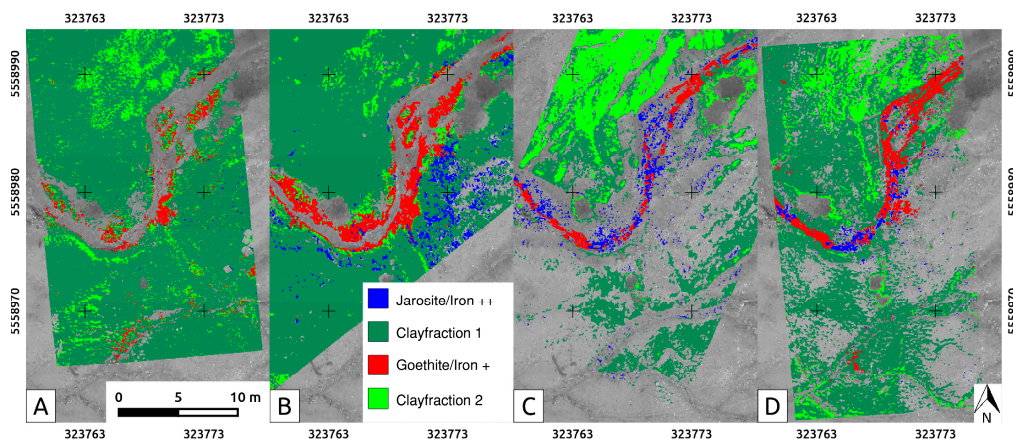

Figure 9. The SAM classification with the four endmembers is applied for scenes from the four campaigns, involving the same surface feature. The legend is applicable for all four images. (**A**) April; (**B**) May; (**C**) July; and (**D**) September.

The SAM classification on this scene captures the clay zone and coatings of the endmembers goethite and jarosite. During the field trip in May, the water table was observed to be slightly lower than in April. Possibly a thin coating of AMD minerals precipitated on the drained beach parts. The stream feature running through frames C and D is a small erosion rill with minimal water flow. The jarosite endmember with the highest jarosite content was taken in this rivulet. The rivulet was smaller than 5 cm in diameter, and surrounded by oxidized iron coatings, which can be seen in both frames. C and D in Figure 7 illustrate a wall slope, which was carved by erosion.

The results depicted in Figure 9 distribute four scenes from the same area, acquired in four time steps. Frames A–D respectively illustrate campaign months April, May, July, and September. The endmember legend is similar for the four frames. A noticeably difference is the stream, visible as red features in D and C, with differing amounts of pixels indicating jarosite in C, and increased goethite cover in D. The clay fraction is densely mapped in A and B, while in C and D there are broader

gaps in between. Frames A and B indicate a channel seam, which contains endmember goethite. Distinguishable are the small erosion rills in the south of frame D. A larger part in the north is classified as clay-rock endmember (also referred to as sample 2-022), which is observed during field investigation. Possible reasons for the mapping differences are concluded in the following discussion section.

4.6. Rikola Image Spectra

We exhibit exemplary image spectra of Rikola drone-borne data in Figure 10, acquired from two field campaigns, with their locations marked in the respective scenes. The mineral mapping outcome depends on the quality of the image spectra. Each scene pixel can be regarded as one field spectrum. Again, the canyon location was chosen due to its high field sample density and good HSI coverage. The April spectrum has an iron absorption shape, from 750 to 900 nm in both the handheld and the Rikola spectra. Sample 2 from September shows a reflectance peak around 740 nm before declining. We observed peak shifts towards 750 nm, an indicator for AMD or hydrothermal alteration [26]. The UAS April spectra from September contain outliers between 600 and 700 nm in the spectral curve. The reason is the sensor shift of the Rikola instrument. To moderate this issue, we selected bad bands, mostly from 639 to 671 nm before the spline smoothing. This procedure sometimes leads to a visible sill effect in the spectrum's curve, as seen in the April spectra of Figure 10.
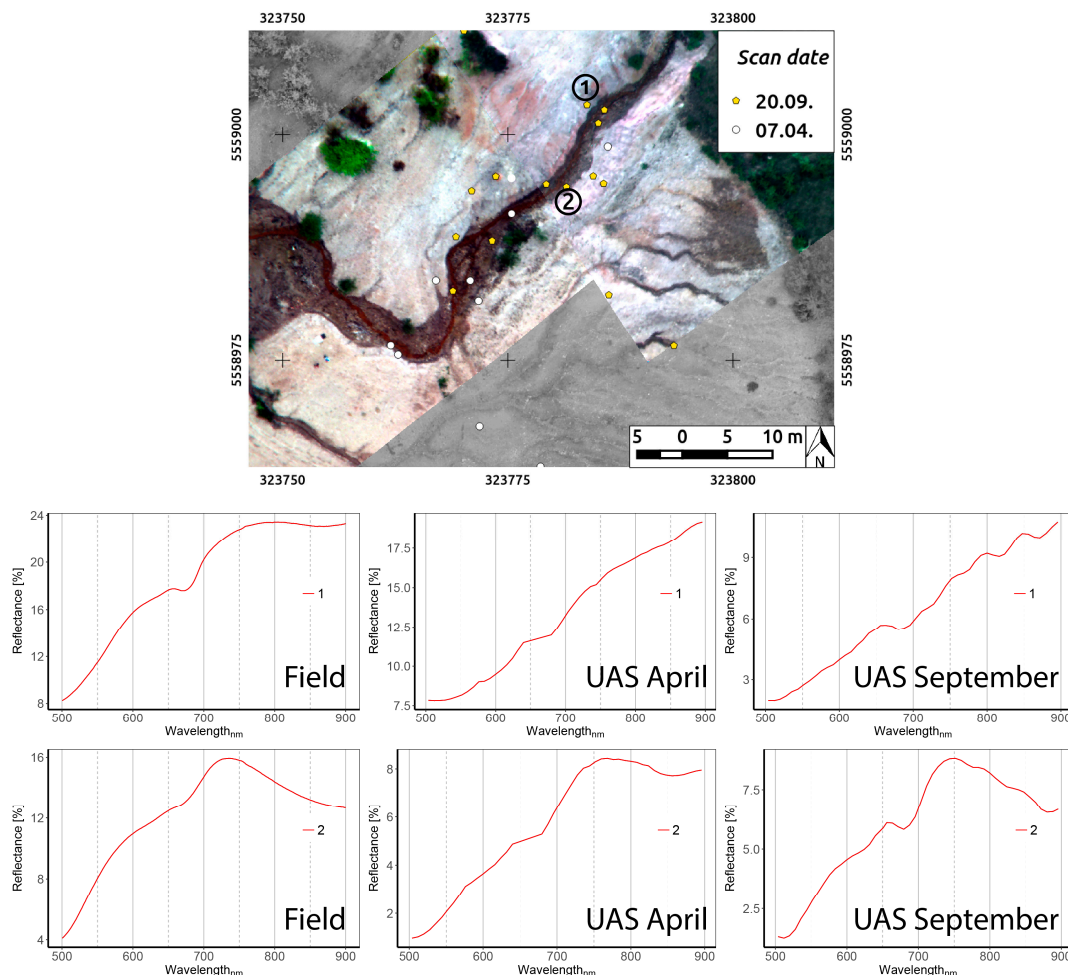

Figure 10. Extracted spectra from UAS-borne HSIs displayed in the two rows below the overview map. The first column (field) depicts a ground spectrum, juxtaposed to it are two spectra extracted from the same location, taken from ROIs of only several pixels. The corresponding spots are marked in the map as numbers **1** and **2**, respectively. The white and yellow points indicate ground truth measurements (pH, field spectroscopy, sampling for iron content).

5. Discussion

Our survey of the Litov site succeeds in the application of a variety of non-invasive investigation methods from remote sensing and applies surface sampling for ground-truth. High-resolution HSIs capture the spatial distribution of AMD minerals in a defined area, set over a course of several months. Figure 11 shows a combination of AMD detection results for one month.
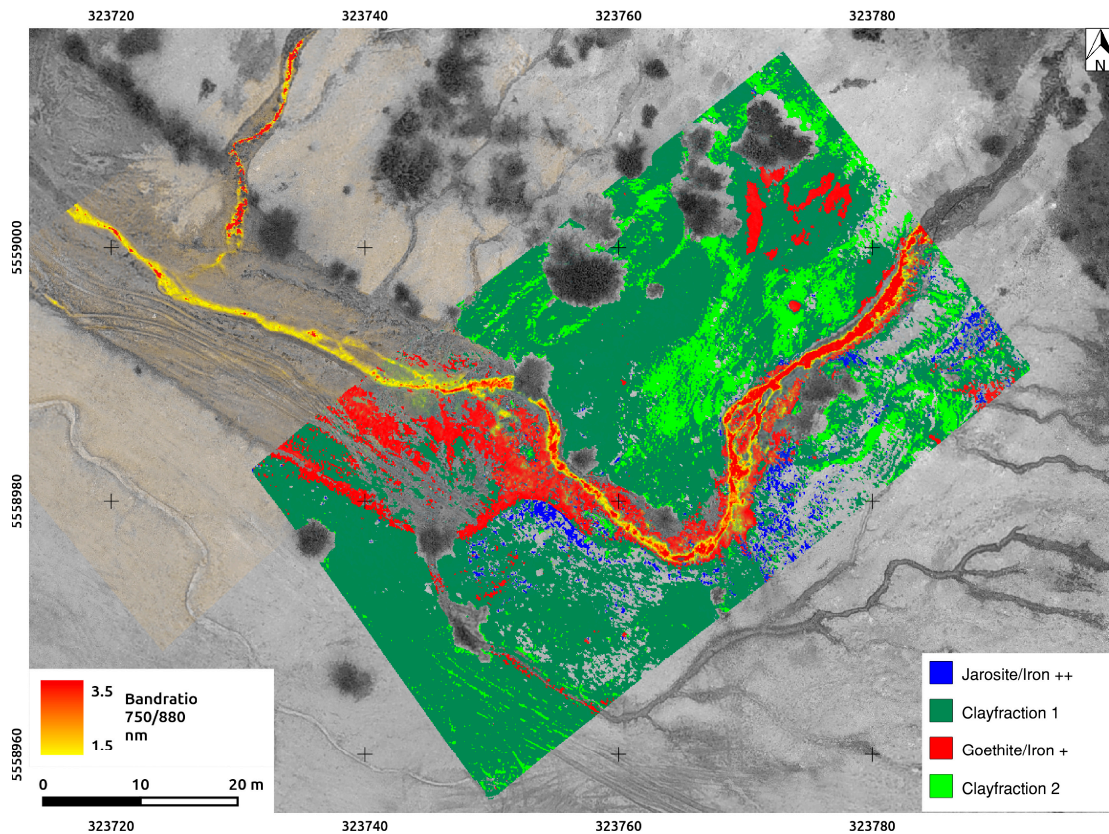

Figure 11. The combined result of three HSIs combined. The overlaid image is of a Rikola band-ratio (May) of 750/880 nm, highlighting only the stream. The second applied method is the SAM classification (May) with the endmember library as the target spectra. The high HSI resolution (5 cm) enables detailed mapping, thus accentuating the iron crusts bordering the stream. The combination of the two methods reveals a conclusive picture of the mapping capability of Rikola HSIs.

5.1. Evaluation and Relation of pH, Iron, and HSI

We compare between pH values, geochemistry values, field-spectroscopy, and drone-borne data. The resulting indication is a number of correlations, as seen in Figure 12. Yet, a high R^2 does not explain causation from correlation [49]. Causation is often asymmetric, but correlations are symmetric. For instance, a low pH value can explain AMD-related minerals, but detection of jarosite or high iron content does not explain low pH values in the same sample. Often the causes are a reason of several underlying variables.

For an excerpt of possible correlations, see Figure 12. As the pH scale is logarithmic, Fe and S values were logarithmized for consistency. The correlation between pH–log Fe is non-significant, the correlation between pH–log S ($R^2 = 0.67$; $p < 0.05$) implies a significant correlation. This means that for low pH values, higher S values occur, indicating AMD minerals containing S (such as jarosite) to some degree. XRF gradients for Fe indicates that the element is omnipresent in the samples and, therefore, its influence among the variables is valued low.

We observe a positive trend between pH value and the Fe–S ratio (R^2 = 0.52; $p < 0.05$). The pH ranged from 2.5–3 correlates to low Fe–S ratios, an indicator for jarosite. A relationship between handheld spectroscopy and the Rikola band-ratio is derived from position of the 900 nm iron absorption feature. The data indicates that a shift of the 900 nm feature correlates with a higher band ratio, presumably resulting from intensive iron absorption features.

Most importantly, we observed a positive high correlation (R^2 = 0.75; $p < 0.05$) between Fe (wt %) from surface pXRF measurements and the UAS-borne Fe-band ratio (720/880 nm), calculated from the HSI of AMD-influenced areas. In Figure 12, the correlation is visible, showing the gradient between physical ground-truth and spectral data. This observation shows that different iron contents are visible in UAS HIS data.
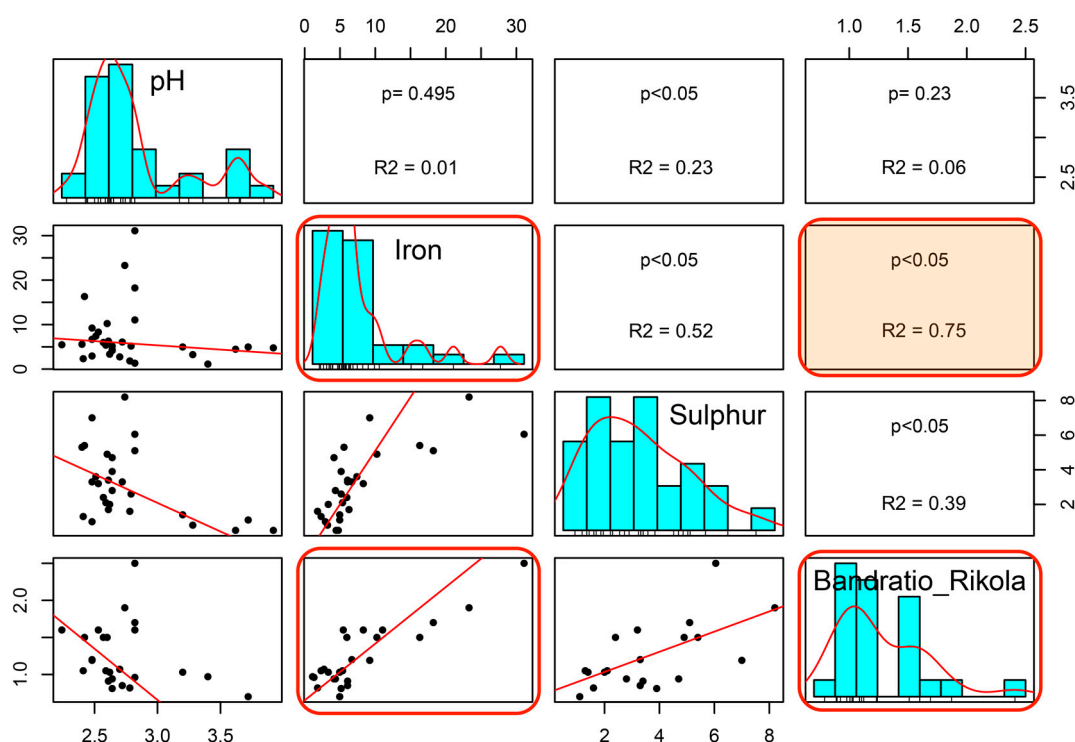

Figure 12. Extracted point values depicting the linear relationships between measured pH, iron and sulfur contents (XRF measurements in wt %) and the Rikola band ratio. The iron band ratio (720/880 nm) trend shows a linear correlation with ground measured Iron. Band ratio values >1.0 indicate iron minerals on the surface. Plotted p values and R^2 values indicate linear correlations among the data.

5.2. Evaluation of Spectral Classification Results

We consider that, during the identification with SAM for single spectra, it occurs that materials and minerals are identified, which in reality are not present in the area. During the spectral inspection of clay fractions, for instance the minerals nontronite, kaolinite, and smectite were suggested by the USGS database. XRD analysis of said samples confirmed only kaolinite and smectite. The high abundance of clays in the HSIs and their lack of spectral features allowed only for two principal clay distinctions. Therefore, and in conclusion with XRF sampling, sample 2-022 as an endmember for clay fraction 2, locally mixed between AMD iron crusts and rocks. Clay fraction 1 (2-029) as the representative endmember for the most abundant clay sheet-silicate fraction, was referred to as clay fraction 1. The XRD results propose 7% of jarosite, but its fingerprint remains hidden in the reflectance spectra. The jarosite features are covered by major clay absorption properties. Thus, jarosite is in mixture with the low-pH clays of the mud fan. Precedent results were already described as

the idealized mineral bulls-eye [1] of pyrite-rich mine wastes. The USGS library spectra for the iron oxide minerals mostly resulted from powder samples. This processing step has an influence on the shift of the electron transition properties for the absorption features. Still, our classification results illustrated a high correlation (SAM classification values <0.08 rad applied on UAS HSI) between field and airborne spectra, especially in the absorption area from 650 to 900 nm, which is crucial for AMD mineral detection and separation. We observe this high fit (see Figure 12) in the correlation between the UAS-HSI relative band intensity for Fe and the physical Fe reading (XRF-wt %). Especially, the seams around the tributary presented well-developed iron crusts in the classifications, which were observed in the field as well. For extraction of iron features, single scenes were used instead of mosaicked HSIs. The illumination differences from one Rikola HSI to the next can change rapidly, for one cloud may change the light-conditions drastically between two image acquisitions in seconds. Furthermore, all the investigated absorption features are visible in single scenes, which cover sufficient space to map relevant AMD features. The achieved HSI resolution reached 3 cm pixel size. For example, the Rikola laboratory classifications on Figure 3 resemble at least 3×3 pixels in an HSI from September.

While the classification results are consistent, a drawback is the cut at 900 nm for the Rikola spectra. Consequently, the goethite/hematite maximum absorption depth around 920 nm cannot be observed in Rikola images, solely in the field spectra. The acquired laboratory Rikola spectra, serving as endmembers, classify small spectral differences. The sensor shift around 650 nm in the Rikola is a disadvantage, to cope with this several bands around this shift were removed. The effect can be seen in the goethite shoulder around 674 nm and, to a higher degree, the jarosite-shoulder at 650 nm is obscured by this shift in Rikola spectra. Determining for the reliability of the Rikola classifications is the whole preprocessing chain [12]. While the initial processing steps are fixed, they require accurate input and weighting by the user. The local features on the orthophotos have to be similar to the Rikola images, otherwise the automatic geo-referencing can fail.

For the topographic correction, the DEM should have a high resolution, preferably in the range of the Rikola HSIs. The topographic illumination normalizations required us to decide for the applied method, before and after critical investigation of the images. Artefacts and distortions can occur, depending on the solar incidence properties and the applied method. The final step in the image processing chain, the empirical line calibration, requires good visible calibration targets in the field and the HSI. For the calibration, the black and grey panel presented reliable results. Calibration with the white panel led to over-saturations in the image. Reflectance spectra in these HSIs reached values over 100%, so we rejected the white target in most cases. As HSIs are obtained band-wise in single steps, illumination conditions may change during flight time. Several sets of calibration panels in the field could cope with changing light conditions.

We applied accuracy assessment for the classifications for HSI of the September campaign. Two areas (500 pixel each) from the canyon (Figure 9D) are selected as known reference standard for the supervised classification. These standards feature goethite and clays, clearly visible stream features. We used a maximum likelihood classifier on the HSI. A comparison with the library-based SAM classification showed an overall accuracy of 75% ($\kappa = 0.65$).

5.3. Image Quality Evaluation

We found the HSI quality of the April and September datasets as satisfying. For April data, four poor bands were designated around 650 nm. The September spectra show a small sinusoidal shape from 800 to 900 nm (Figure 10. UAS September). The image quality of HSIs from July was influenced by increased noise and the spectral quality is degraded by low reflection. On the contrary, the May HSI yielded compelling spectra in regard to the SNR and feature abundances (Figure 6D). We preferred the SAM classifier approach as preferential algorithm for trustworthy classifications. Other, more sophisticated methods (e.g., SFF, random classifiers) tend to over-classify larger areas of the AMD-influenced river area. We applied smoothing and bad band designation carefully, at some point the overcorrection may create spectra that appear fitting, but do not represent the true physical properties of the actual surface. An improvement for drone-borne mapping could be yielded by camera

systems with a broader wavelength range, e.g., from 350–1000 nm. HS cameras with increased SNR will lead to clearer spectral response. Increased research about the relation of morphology and HSI will be possible, in order to explain the encountered AMD mineral distribution. The HSI never suffered larger image distortions or artefacts, due to the stop-and-go motion of the UAS.

5.4. Sampling Results

We treated XRF readings more as a gradient rather than actual measurements. Especially, XRF values for elements found below iron in the periodic table should not be treated as quantitative amounts, but more in a conceptual way as a trend highlighter, which can decline or incline. Sample inhomogeneity during their laboratory scanning influences the wt % values. The calibration of detected materials and their LOD strongly depends on reference material content.

By contrast, the XRD results, giving representative mineral contents with Rietveld refinement, are used for qualitative statements. It could be proved that jarosite and goethite are abundant in the field as the main iron-bearing minerals. We found small amounts of hematite in association with jarosite as well. Schwertmannite, which we expected to see [34] could not be traced. However, with pH values above 3.0 and well-developed iron crusts in the whole Litov area, occurrences of schwertmannite cannot be ruled out. The importance to categorize this mineral came from its possible indication by field spectroscopy. Detected minerals from XRD, however, do not represent the actual surface properties, as the sample material comes from a larger bulk, from soil depths several centimeters deep, whereas hyperspectral data represents only the first few microns of the surface. The deeper lying oxidizing zone might contain different materials.

5.5. The Influence of Regional Precipitation

The recorded precipitation over the time of the four campaigns is displayed in Figure 13. We compared monthly mean precipitation values for this station with the 2016 data for the time between April and September. The recorded precipitation for this time-period is slightly above the monthly mean values. Accordingly, an influence on the classifications could arise from higher precipitation values in July before campaign 3. Before campaign 4, three days with increased rainfall are recorded. The time period before campaign 1 and 2 was dry with small rain events, compared to the monthly average. Mapping results could be altered, due to wet surfaces and puddles covering relevant AMD features. A possible reason for the hidden stream feature of classification in Figure 9 might be a differing amount of debris and a change of water table in the river, as well as the changed iron content in the water, similar to investigations on Leviathan Lake [29].
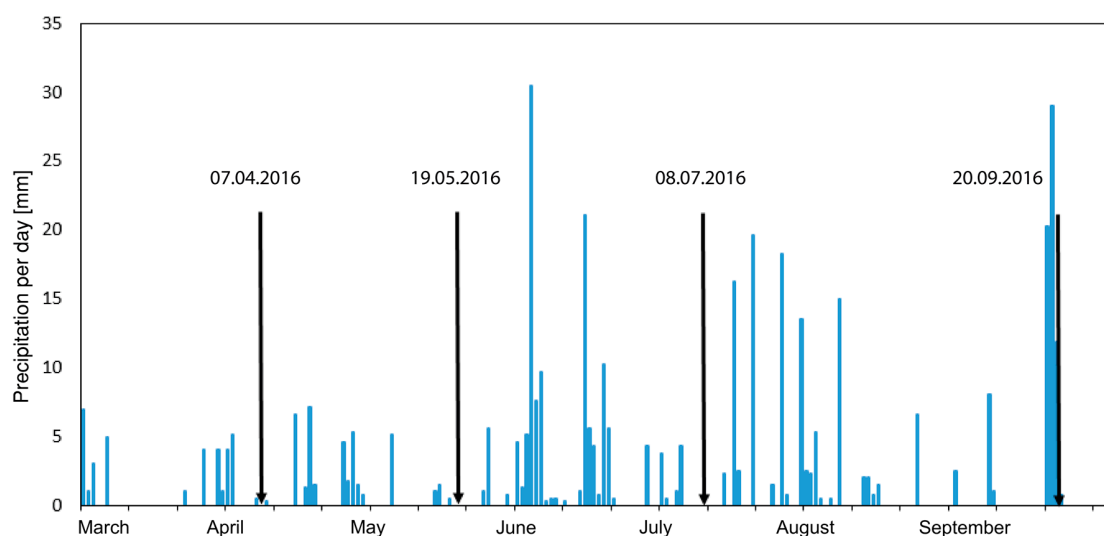

Figure 13. Precipitation records from the Czech meteorological service over the course of the study. Data from recording station Cheb. The black arrows specify to the dates of the field campaigns.

5.6. The Gap between Satellite, Airborne and Drone-Borne Data

With the introduction of UAS in combination with hyperspectral sensor equipment, we achieved sub-decimeter image resolution for drone-borne data aiming for mineral detection. Moreover, the outline of this study was set-up as proof of concept. The influencing limitations of UAS in the civil sector are still endurance, workload capacity, and legal regulations. Henceforth, they cannot substitute common remote sensing tools, such as satellite and airborne platforms. However, provided that these platforms operate at altitudes of kilometers and up to orbital distances, we still see an extended gap between sensors and ground targets. UASs offer new insights in regard to data resolution and precision. The achieved accuracies allow us to use the calibrated spectral signal without pixel un-mixing. Notably, the flight altitudes of 40–60 m mitigates atmospheric aspects in the spectral response. Small effects of the atmosphere are reduced by comparing the spectral response at the UAS to the ground reference spectra, using the empirical line correction. The reference panels should always be at the same distance and orientation to the sensor as the target features.

6. Conclusions

Our study confirms that detection and precise mapping of AMD-related iron minerals based on UAS-borne HSIs is feasible. Based on a multi-temporal dataset from the Sokolov region, the combination of hyperspectral field and laboratory data was proven successful in terms of mineral detection. We utilized DSMs and point clouds created by SfM-MVS photogrammetry for topographic image corrections and supporting the classifications using morphological properties. A diagnostic endmember spectral library was constructed for the supervised classification and validation. Classified HSI are able to depict iron-bearing minerals (hardpans) at cm-resolution (R^2 = 0.75 for in-situ measured iron, correlated to UAS-borne iron mapping). This high resolution creates the opportunity to distinguish features usually not visible even in airborne remote sensing data. We proved the spectral distinction of two different AMD minerals, goethite and jarosite. Results indicate that both minerals were found in association, as indicated by mapping, mineralogy, and literature comparisons, in this region.

Nonetheless, a careful preprocessing is indispensable before analyzing HSIs. Mapping results indicate that the overall surface conditions did not change to a significant degree in the classified area. A small canyon located on the tailing showed a higher degree of alteration, visible in the SAM classification. Small mineral variations are visible, bordering the stream seams in the canyon area, whereas the pH value did not change significantly during the observed time-period. We created reproducible results of high-resolution drone-borne images. We can state that drone operations demand significantly less time and investment, once the initial expenses for equipment are overcome. Flexible application of UAS shortens campaign planning times. We found a pH prediction from drone-borne data alone is valid but limited to relative estimations. The amount of limiting conditions is quite diverse, in order to produce a precise pH. Additionally, we show the multi-scale approach of this study as a promising utilization of UAS for geo-hydrological mapping in the timespan of months.

As an interdisciplinary approach our study demonstrates the benefits of coupling state-of-the-art remote sensing techniques for environmental monitoring. The promising results for AMD mineral maps and laboratory examinations could further be correlated to hydrologic models and 3D surface maps of the study areas. Eventually UAS-based hyperspectral remote sensing will close the apparent observational gap between airborne remote sensing and ground-based field work.

Author Contributions: R.J., R.Z., S.L., and R.G. contributed in a substantial way to the field experiments; R.Z. conducted UAS flights and surveying; S.L. designed the processing toolbox; R.J. analyzed and evaluated the data and designed the experimental workflow; R.M. contributed to the mineralogical analysis. R.J. wrote the

manuscript. And R.G. provided background knowledge of remote sensing, reviewed the paper, and gave guidance and advice during all stages. All authors contributed by editing parts of the manuscript.

Conflicts of Interest: The authors declare no conflict of interest.

References

1. Swayze, G.A.; Smith, K.S.; Clark, R.N.; Sutley, S.J.; Pearson, R.M.; Vance, J.S.; Hageman, P.L.; Briggs, P.H.; Meier, A.L.; Singleton, M.J.; et al. Using Imaging Spectroscopy to Map Acidic Mine Waste. *Environ. Sci. Technol.* **2000**, *34*, 47–54. [CrossRef]
2. Wolkersdorfer, C.; Younger, P.L.; Bowell, R. PADRE—Europäische Partnerschaft Für Die Sanierung Saurer Grubenwässer (Partnership for Acid Drainage Remediation in Europe). *Wiss. Mitt.* **2006**, *31*, 213–217.
3. Lottermoser, B.G. *Mine Wastes: Characterization, Treatment and Environmental Impacts*; Springer-Verlag: Berlin/Heidelberg, Germany, 2010.
4. Mielke, C.; Boesche, N.K.; Rogass, C.; Kaufmann, H.; Gauert, C.; de Wit, M. Spaceborne Mine Waste Mineralogy Monitoring in South Africa, Applications for Modern Push-Broom Missions: Hyperion/OLI and EnMAP/Sentinel-2. *Remote Sens.* **2014**, *6*, 6790–6816. [CrossRef]
5. Kruse, F.A.; Boardman, J.W.; Huntington, J.F. Comparison of Airborne Hyperspectral Data and EO-1 Hyperion for Mineral Mapping. *IEEE Trans. Geosci. Remote Sens.* **2003**, *41*, 1388–1400. [CrossRef]
6. Zabcic, N.; Rivard, B.; Ong, C.; Miiller, A.; Exploration, C.; Avenue, D.P. Using Airborne Hyperspectral Data to Characterize the Surface pH of Pyrite Mine Tailings. In Proceedings of the Hyperspectral Image and Signal Processing: Evolution in Remote Sensing, Grenoble, France, 26–28 August 2009; IEEE: Piscataway, NJ, USA, 2009; pp. 4–7.
7. Riaza, A.; Buzzi, J.; García-Meléndez, E.; Carrère, V.; Müller, A. Monitoring the Extent of Contamination from Acid Mine Drainage in the Iberian Pyrite Belt (SW Spain) Using Hyperspectral Imagery. *Remote Sens.* **2011**, *3*, 2166–2186. [CrossRef]
8. Crowley, J.K.; Williams, D.E.; Hammarstrom, J.M.; Piatak, N.; Chou, I.-M.; Mars, J.C. Spectral Reflectance Properties (0.4–2.5 Mm) of Secondary Fe-Oxide, Fe-Hydroxide, and Fe-Sulphate-Hydrate Minerals Associated with Sulphide-Bearing Mine Wastes. *Geochem. Explor. Environ. Anal.* **2003**, *3*, 219–228. [CrossRef]
9. Choe, E.; van der Meer, F.; van Ruitenbeek, F.; van der Werff, H.; de Smeth, B.; Kim, K.W. Mapping of Heavy Metal Pollution in Stream Sediments Using Combined Geochemistry, Field Spectroscopy, and Hyperspectral Remote Sensing: A Case Study of the Rodalquilar Mining Area, SE Spain. *Remote Sens. Environ.* **2008**, *112*, 3222–3233. [CrossRef]
10. Montero, S.I.C.; Brimhall, G.H.; Alpers, C.N.; Swayze, G.A. Characterization of Waste Rock Associated with Acid Drainage at the Penn Mine, California, by Ground-Based Visible to Short-Wave Infrared Reflectance Spectroscopy Assisted by Digital Mapping. *Chem. Geol.* **2005**, *215*, 453–472. [CrossRef]
11. Honkavaara, E.; Eskelinen, M.A.; Polonen, I.; Saari, H.; Ojanen, H.; Mannila, R.; Holmlund, C.; Hakala, T.; Litkey, P.; Rosnell, T.; et al. Remote Sensing of 3-D Geometry and Surface Moisture of a Peat Production Area Using Hyperspectral Frame Cameras in Visible to Short-Wave Infrared Spectral Ranges Onboard a Small Unmanned Airborne Vehicle (UAV). *IEEE Trans. Geosci. Remote Sens.* **2016**, *54*, 5440–5454. [CrossRef]
12. Aasen, H.; Burkart, A.; Bolten, A.; Bareth, G. Generating 3D Hyperspectral Information with Lightweight UAV Snapshot Cameras for Vegetation Monitoring: From Camera Calibration to Quality Assurance. *ISPRS J. Photogramm. Remote Sens.* **2015**, *108*, 245–259. [CrossRef]
13. Roosjen, P.P.J.; Suomalainen, J.M.; Bartholomeus, H.M.; Clevers, J.G.P.W. Hyperspectral Reflectance Anisotropy Measurements Using a Pushbroom Spectrometer on an Unmanned Aerial Vehicle-Results for Barley, Winter Wheat, and Potato. *Remote Sens.* **2016**, *8*, 909. [CrossRef]
14. Jakob, S.; Zimmermann, R.; Gloaguen, R. The Need for Accurate Geometric and Radiometric Corrections of Drone-Borne Hyperspectral Data for Mineral Exploration: MEPHySTo-A Toolbox for Pre-Processing Drone-Borne Hyperspectral Data. *Remote Sens.* **2017**, *9*, 88. [CrossRef]
15. Colomina, I.; Molina, P. Unmanned Aerial Systems for Photogrammetry and Remote Sensing: A Review. *ISPRS J. Photogramm. Remote Sens.* **2014**, *92*, 79–97. [CrossRef]
16. Hruska, R.; Mitchell, J.; Anderson, M.; Glenn, N.F. Radiometric and Geometric Analysis of Hyperspectral Imagery Acquired from an Unmanned Aerial Vehicle. *Remote Sens.* **2012**, *4*, 2736–2752. [CrossRef]

17. Murfitt, S.L.; Allan, B.M.; Bellgrove, A.; Rattray, A.; Young, M.A.; Ierodiaconou, D. Applications of Unmanned Aerial Vehicles in Intertidal Reef Monitoring. *Sci. Rep.* **2017**, *7*, 1–11. [CrossRef] [PubMed]

18. Jaud, M.; Le Dantec, N.; Ammann, J.; Grandjean, P.; Constantin, D.; Akhtman, Y.; Barbieux, K.; Allemand, P.; Delacourt, C.; Merminod, B. Direct Georeferencing of a Pushbroom, Lightweight Hyperspectral System for Mini-UAV Applications. *Remote Sens.* **2018**, *10*, 204. [CrossRef]

19. Adão, T.; Hruška, J.; Pádua, L.; Bessa, J.; Peres, E.; Morais, R.; Sousa, J.J. Hyperspectral Imaging: A Review on UAV-Based Sensors, Data Processing and Applications for Agriculture and Forestry. *Remote Sens.* **2017**, *9*, 1110. [CrossRef]

20. Adar, S.; Notesco, G.; Brook, A.; Livne, I.; Rojik, P.; Kopačková, V.; Zelenkova, K.; Misurec, J.; Bourguignon, A.; Chevrel, S.; et al. Change Detection over Sokolov Open-Pit Mining Area, Czech Republic, Using Multi-Temporal HyMAP Data (2009–2010). *SPIE Remote Sens.* **2011**, *8180*, 9.

21. Kopačková, V. Using Multiple Spectral Feature Analysis for Quantitative pH Mapping in a Mining Environment. *Int. J. Appl. Earth Obs. Geoinf.* **2014**, *28*, 28–42. [CrossRef]

22. Kopačková, V.; Chevrel, S.; Bourguignon, A.; Rojík, P. Application of High Altitude and Ground-Based Spectroradiometry to Mapping Hazardous Low-pH Material Derived from the Sokolov Open-Pit Mine. *J. Maps* **2012**, *8*, 220–230. [CrossRef]

23. Murad, E.; Rojík, P. Jarosite, schwertmannite, goethite ferrihydrite and lepidocrocite: the legacy of coal and sulfide ore mining. *SuperSoil* **2004**, *3*, 5–9.

24. Kopačková, V.; Hladíková, L. Applying Spectral Unmixing to Determine Surface Water Parameters in a Mining Environment. *Remote Sens.* **2014**, *6*, 11204–11224. [CrossRef]

25. Bigham, J.M.; Schwertmann, U.; Pfab, G. Influence of pH on Mineral Speciation in a Bioreactor Simulating Acid Mine Drainage. *Appl. Geochem.* **1996**, *11*, 845–849. [CrossRef]

26. Hunt, G.R.; Ashley, R.P. Spectra of Altered Rocks in the Visible and near Infrared. *Econ. Geol.* **1979**, *74*, 1613–1629. [CrossRef]

27. Bishop, J.L.; Murad, E. The Visible and Infrared Spectral Properties of Jarosite and Alunite. *Am. Mineral.* **2005**, *90*, 1100–1107. [CrossRef]

28. Bigham, J.M.; Schwertmann, U.; Traina, S.J.; Winland, R.L.; Wolf, M. Schwertmannite and the Chemical Modeling of Iron in Acid Sulfate Waters. *Geochim. Cosmochim. Acta* **1996**, *60*, 2111–2121. [CrossRef]

29. Davies, G.E.; Calvin, W.M. Quantifizierung Der Eisenkonzentration von Synthetischer Und in Situ Vorkommender Saurer Bergbaudränage: Eine Neue Technik Unter Nutzung Tragbarer Feldspektrometer. *Mine Water Environ.* **2017**, *36*, 299–309. [CrossRef]

30. Jordan, C.J.; Chevrel, S.; Coetzee, H.; Ben-Dor, E.; Ehrler, C.; Fischer, C.; Grebby, S.R.; Kerr, G.; Livne, I.; Kopačková, V.; et al. EO-MINERS: Monitoring the Environmental and Societal Impact of the Extractive Industry Using Earth Observation. In Proceedings of the 2013 IEEE International Geoscience and Remote Sensing Symposium (IGARSS), Melbourne, VIC, Australia, 21–26 July 2013; 1741–1744.

31. Denk, M.; Glaesser, C.; Kurz, T.H.; Buckley, S.J.; Drissen, P. Mapping of Iron and Steelwork by-Products Using Close Range Hyperspectral Imaging: A Case Study in Thuringia, Germany. *Eur. J. Remote Sens.* **2015**, *48*, 489–509. [CrossRef]

32. Ziegler, P.A. European Cenozoic Rift System. *Tectonophysics* **1992**, *208*, 91–111. [CrossRef]

33. Rojík, P. New Stratigraphic Subdivision of the Tertiary in the Sokolov Basin in Northwestern Bohemia. *J. Czech Geol. Soc.* **2004**, *49*, 173–185.

34. Murad, E.; Rojík, P. Iron Mineralogy of Mine-Drainage Precipitates as Environmental Indicators: Review of Current Concepts and a Case Study from the Sokolov Basin, Czech Republic. *Clay Miner.* **2005**, *40*, 427–440. [CrossRef]

35. Kupková, L.; Potuckova, M.; Zachová, K.; Lhtáková, Z.; Kopačková, V.; Albrechtová, J. Chlorophyll Determination in Silver Birch and Scots Pine Foliage from Heavy Metal Polluted Regions Using Spectral Reflectance Data. *EARSeL eProc.* **2012**, *11*, 64–73.

36. Van der Meer, F.D.; van der Werff, H.M.A.; van Ruitenbeek, F.J.A.; Hecker, C.A.; Bakker, W.H.; Noomen, M.F.; van der Meijde, M.; Carranza, E.J.M.; de Smeth, J.B.; Woldai, T. Multi- and Hyperspectral Geologic Remote Sensing: A Review. *Int. J. Appl. Earth Obs. Geoinf.* **2012**, *14*, 112–128. [CrossRef]

37. Makelainen, A.; Saari, H.; Hippi, I.; Sarkeala, J.; Soukkamaki, J. 2D Hyperspectral Frame Imager Camera Data in Photogrammetric Mosaicking. *Int. Arch. Photogramm. Remote Sens. Spat. Inf. Sci.* **2013**, *XL-1/W2*, 263–267. [CrossRef]

38. Savitzky, A.; Golay, M.J.E. Smoothing and Differentiation of Data by Simplified Least Squares Procedures. *Anal. Chem.* **1964**, *36*, 1627–1639. [CrossRef]

39. *Spectralon Technical Datashet-Reflectance Materials and Coatings*; Technical guide; Labsphere: North Sutton, NH, USA, 2016; pp. 1–26.

40. *PhotoScan Professional Version 1.2.5*; Agisoft LLC: St. Petersburg, Russia, 2016.

41. *Soil Quality—Determination of pH 10390:2005. 13.080.10—Chemical characteristics of soils*; DIN-ISO Technical Committee ISO/TC 190-SC 3: Bad Mergentheim, Germany, 2005.

42. Tucker, C.J. Red and Photographic Infrared Linear Combinations for Monitoring Vegetation. *Remote Sens. Environ.* **1979**, *8*, 127–150. [CrossRef]

43. Kruse, F.A.; Lefkoff, A.B.; Boardman, J.W.; Heidebrecht, K.B.; Shapiro, A.T.; Barloon, P.J.; Goetz, A.F.H. The Spectral Image Processing System (SIPS)—Interactive Visualization and Analysis of Imaging Spectrometer Data. *Remote Sens. Environ.* **1993**, *44*, 145–163. [CrossRef]

44. Younger, P.L.; Banwart, S.; Hedin, R.S. *Mine Water: Hydrology, Pollution, Remediation*; Springer: Dordrecht, The Netherlands, 2002; Volume 53.

45. *S1 Titan Model 600/800 GeoChem Data Sheet*; Bruker: Berlin, Germany, 2014.

46. *Brammer Standards Geological Materials Catalogue*; Brammer Standard Company Inc.: Houston, Texas, USA, 2014.

47. Clark, R.N.; Swayze, G.A.; Wise, R.; Livo, E.; Hoefen, T.; Kokaly, R.; Sutley, S.J. *USGS Digital Spectral Library Splib06a*; U.S. Geological Survey: Reston, VA, USA, 2007.

48. Hubbard, B.E.; Crowley, J.K.; Zimbelman, D.R. Hyperion, ALI, and ASTER Imagery. *Comp. Gen. Pharmacol.* **2003**, *41*, 1401–1410.

49. Aldrich, J. Correlations Genuine and Spurious in Pearson and Yule. *Stat. Sci.* **1995**, *10*, 364–376. [CrossRef]